symmetry

MDPI

Article

Numerical Simulation of Conjugate Mixed Convection in 3D Channel with Heat-Generating Flat Element and Symmetrical Solid Two-Fin System

Nikita S. Gibanov and Mikhail A. Sheremet *

Laboratory on Convective Heat and Mass Transfer, Tomsk State University, Tomsk 634050, Russia; gibanov@mail.tsu.ru

* Correspondence: sheremet@math.tsu.ru; Tel.: +7-3822-529740

Abstract: This paper presents the numerical simulation results of conjugate mixed convection in a three-dimensional channel with a heat-generating element and solid fins. It should be noted that the symmetrical location of fins has been studied. The system of partial differential equations, presented in dimensionless form using velocity and vorticity vectors, has been solved by the finite difference method on a uniform grid. The central difference schemes have been used to approximate diffusive terms. In contrast, for an approximation of convective terms, the monotonic Samarskii difference schemes have been applied to improve the stable properties of central differences of the second order of accuracy. Analysis has been performed on a wide range of governing parameters, including the Reynolds number ($200 \leq Re \leq 1000$), the material of the fins (aluminum, copper, and iron), and the location of the fins on the heater surface, taking into account the identical distances between the fins and the nearest walls. Water has been considered a working cooling medium. The obtained outcomes characterize the most efficient heat removal from the surface of the energy source using the considered fin system. For example, by using copper fins, the cooling efficiency of the heating element can be increased. The average heater temperature decreases significantly with an increase in the Reynolds number. The distance between the fins also makes a significant contribution to the cooling phenomenon. It is noted that with the most successful choice of location, it is possible to decrease the temperature of the heater by more than 12%.

Keywords: conjugate mixed convection; local heat-generating source; three-dimensional channel; solid fins; finite difference method

Citation: Gibanov, N.S.; Sheremet, M.A. Numerical Simulation of Conjugate Mixed Convection in 3D Channel with Heat-Generating Flat Element and Symmetrical Solid Two-Fin System. *Symmetry* **2023**, *15*, 1467. https://doi.org/10.3390/sym15071467

Academic Editor: Bilen Emek Abali

Received: 21 May 2023
Revised: 2 July 2023
Accepted: 13 July 2023
Published: 24 July 2023

1. Introduction

Currently, the problems of cooling and optimization of various complex engineering systems are very relevant [1]. Various types of cooling systems are being developed, starting with passive systems, which are undoubtedly one of the most common but have a limit on the amount of heat flux they can effectively remove. Active cooling systems are most often used along with passive cooling systems, which are more efficient but have limitations.

Since the experiments on fluid flow through a thin cylindrical tube by Hagen in 1839 [2] and Poiseuille in 1846 [3], which subsequently degenerated into the Hagen–Poiseuille flow law, a lot of numerical and experimental work has been carried out. These studies have focused on liquid flows in channels and cavities with heaters of various cross-sections and geometric dimensions and under the influence of various complicating effects [4–22]. Thus, Sáchica et al. [4] have numerically investigated the mixed convective heat exchange of a nanofluid (aluminum oxide–water) with consideration of the magnetic field in a vertical channel with two square cavities, the side boundaries of which have been heated. The results indicate that the dynamics of vortices, heat transfer characteristics, and the magnitude of the irreversibility of entropy generation are influenced by the strength of the applied magnetic field and the volume fraction of nanoparticles. Qureshi et al. [5]

have studied the flow of a hybrid nanofluid in a horizontal channel with an obstacle. It is shown that with an increase in the radius of the obstacle, the heat transfer in the channel increases by 119%. Huang et al. [6] have performed a numerical study of the flow in a channel with heating elements and porous inserts to improve the cooling efficiency. It has been found that recirculation induced by porous blocks significantly improves heat transfer, both on the upper and right walls of the second and subsequent blocks. Premachandran and Balaji [7] have numerically scrutinized the conjugate convective–radiative heat transfer in a horizontal channel with protruding energy sources. The influence of Reynolds number, Grashof number, relative thermal conductivity, and surface radiation on fluid flow and heat transfer has been analyzed. A correlation for a dimensionless maximum temperature is developed using the method of asymptotic expansions. The mixed convection of nanofluid in a channel with partitions alternately located on the walls under the influence of a magnetic field has been numerically investigated by Ali et al. [8]. The area on the lower wall of the channel is heated, and the remaining walls are insulated. The intensity of the flow increases with an increase in the Reynolds number and decreases with an increase in the strength of the magnetic field and the concentration of nanoparticles. The heat transfer efficiency decreases by 22.14% at $Ha = 50$ compared to $Ha = 0$. The heat transfer rate in a working liquid with 5% nanoparticles is 33.86% higher than in water as a base liquid. Yerramalle et al. [9] have studied numerically the mixed convection in a horizontal channel having a heat source on the lower wall and a porous insert partially filling the channel. As a result, the optimal thickness of the porous insert has been established to improve heat transfer efficiency. Moreover, Biswas et al. [16] have analyzed mixed air convection in a ventilated cavity with inlet and outlet ducts and various heated elements using the finite volume method with the SIMPLE algorithm. It has been revealed that in the case of heaters placed on both vertical walls, the incoming air forms two hydrodynamic parts. This illustrates an interaction between the externally forced convective air flows and the inner natural convective air circulations. Biswas et al. [17] have calculated the mixed convection of air in a 2D channel with a cavity having an injection port. The analysis performed has shown that adding the injection port to the bottom wall of the cavity allows for enhanced heat transfer.

Along with numerical works, there are also experimental studies [23–26]. Kamath et al. [23] have conducted experimental studies on mixed convection in a vertical channel with aluminum porous inserts, with porosity values ranging from 0.9 to 0.95. As a result of a multiparametric study, the authors have presented the correlations for the Nusselt number on the wall depending on the Richardson number, Reynolds number, and porosity. Mandev and Manay [24] have investigated experimentally the contribution of natural and forced convection to heat transfer in rectangular stainless steel microchannels with different roughness values. It has been found that surface roughness has a significant effect on mixed convective heat exchange. An increase in surface roughness from 1.1 microns to 1.8 microns in microchannel radiators with cross sections of 300 microns × 300 microns, 700 microns × 300 microns, 300 microns × 450 microns, and 700 microns × 450 microns can lead to an increase in the Nusselt number by 24%, 19%, 17%, and 13%, respectively. Additionally, if the surface roughness further increases from 1.8 microns to 3.0 microns, the Nusselt number increases by 17%, 15%, 14%, and 10%, respectively, for the same cross-sections of the channel. Dogan et al. [25] have considered the mixed convective heat exchange in a rectangular channel with a set of discrete heaters in the lower part of the channel, arranged in eight rows. Distributions of temperature and Nusselt numbers on the surface of energy sources for various Grashof and Reynolds numbers have been obtained. It has been shown that the temperature on the wall's surface with heating zones increases with the growth of the Grashof number. In contrast, the average Nusselt numbers have complicated behavior.

Due to the complexity of modern problems and the need for a complete understanding of all processes occurring in the studied areas, it is necessary to conduct numerical studies as accurately and in as much detail as possible. As a result, special attention should be paid to the numerical modeling of mixed convection problems in spatial objects [27–31].

From the point of view of setting the problem and the required resources, these problems are certainly time-consuming, but the results obtained are as close to reality as possible. That is why such works are the most valuable, but they are carried out much less. Thus, Boulemtafes-Boukadouma et al. [27] have investigated the effect of the channel height on the mixed convection in a solar collector. Constant heat flux was applied to the lower plate range of 200 to 1000 W/m^2, and the Reynolds number was also varied from 50 to 1000. As a result, it has been found that an increase in heat flux does not lead to significant changes in heat transfer and flow intensity at low channel heights. However, at high channel heights, an increase in heat flux enhances the effect of buoyancy in the flow and leads to high turbulence. In addition, an increase in the Reynolds number at low channel heights significantly improves heat transfer. At high channel heights, an increase in the Reynolds number suppresses the ejection forces, and consequently, the Nusselt number decreases. Rhodes et al. [28] have numerically studied 3D flow with a heating zone in a rectangular vertical channel to which a magnetic field is applied perpendicular. It has been shown that an increase in the Grashof number or a decrease in the Reynolds number enhances the buoyancy effect. In contrast, an increase in the Hartmann number leads to a growth in the maximum temperature due to the suppression of turbulence. Danane et al. [29] have analyzed the laminar regimes of mixed convective heat transfer in the flow of a viscoplastic Bingham fluid in a three-dimensional channel with vertical, inclined, and circular reverse ledges. It has been shown that the recirculation zones can be increased with the growth of the pushing forces. Also, the recirculation zones are weakened due to the predominance of viscous forces.

The objective of the present research is a numerical simulation of water-mixed convection in a three-dimensional rectangular horizontal channel with a local flat heater of constant heat flux under the influence of a symmetrical solid two-fin system. The problem considered deals with analyzing the passive cooling systems for the heat-generating elements based on the solid fins. Therefore, the results can be used for optimizing cooling systems for heat-generating elements in electronics, heat exchangers, and power engineering devices. Moreover, this study illustrates applying a mixed theoretical approach to analyze fluid flow and heat transfer. It means that an application of vorticity and velocity vectors can effectively analyze fluid flow and heat transfer in 3D channel geometry.

2. Mathematical Model

Mixed convection is considered in a rectangular horizontal channel of size $L \times H \times H$ ($L = 3H$). The channel features infinitely thin walls and is subjected to an energy source of constant heat flux. Additionally, a symmetrical two-fin system is mounted on the surface of the channel. The analyzed geometry is schematically shown in Figure 1. The working fluid is considered to be Newtonian, thermally conductive, and satisfying the Boussinesq approximation. The energy source is located at a distance of $H/2$ from the entrance to the channel. The side walls of the channel are considered to be adiabatic. A horizontal cooling flow is supplied at the inlet. All wall surfaces are assumed to be impermeable. The thermophysical characteristics of the liquid are constant, and the flow regime is laminar. The solid fins are assumed to be heat-conducting. It is assumed that the fluid flow and heat transfer inside the channel are three-dimensional and that viscous dissipation is neglected. The fins are placed at the heater surface with an identical distance between the fins and the nearest channel wall. Such a symmetrical location of fins allows for analyzing the influence of the distance between the fins on heat transfer performance, excluding possible asymmetrical interactions between the fin surface and channel walls.

The dimensional system of governing equations describing the three-dimensional heat and mass transfer in the considered channel can be written as follows:

- For the liquid zone

$$\frac{\partial u}{\partial x} + \frac{\partial v}{\partial y} + \frac{\partial w}{\partial z} = 0, \quad (1)$$

$$\frac{\partial u}{\partial t}+u\frac{\partial u}{\partial x}+v\frac{\partial u}{\partial y}+w\frac{\partial u}{\partial z}=-\frac{1}{\rho}\frac{\partial p}{\partial x}+\nu\left(\frac{\partial^2 u}{\partial x^2}+\frac{\partial^2 u}{\partial y^2}+\frac{\partial^2 w}{\partial z^2}\right), \tag{2}$$

$$\frac{\partial v}{\partial t}+u\frac{\partial v}{\partial x}+v\frac{\partial v}{\partial y}+w\frac{\partial v}{\partial z}=-\frac{1}{\rho}\frac{\partial p}{\partial y}+\nu\left(\frac{\partial^2 v}{\partial x^2}+\frac{\partial^2 v}{\partial y^2}+\frac{\partial^2 v}{\partial z^2}\right), \tag{3}$$

$$\frac{\partial w}{\partial t}+u\frac{\partial w}{\partial x}+v\frac{\partial w}{\partial y}+w\frac{\partial w}{\partial z}=-\frac{1}{\rho}\frac{\partial p}{\partial z}+\nu\left(\frac{\partial^2 w}{\partial x^2}+\frac{\partial^2 w}{\partial y^2}+\frac{\partial^2 w}{\partial z^2}\right)+g\beta(T-T_0), \tag{4}$$

$$\frac{\partial T}{\partial t}+u\frac{\partial T}{\partial x}+v\frac{\partial T}{\partial y}+w\frac{\partial T}{\partial z}=\alpha_f\left(\frac{\partial^2 T}{\partial x^2}+\frac{\partial^2 T}{\partial y^2}+\frac{\partial^2 T}{\partial z^2}\right) \tag{5}$$

- For the solid fins

$$\frac{\partial T}{\partial t}=\alpha_s\left(\frac{\partial^2 T}{\partial x^2}+\frac{\partial^2 T}{\partial y^2}+\frac{\partial^2 T}{\partial z^2}\right). \tag{6}$$

Further, the non-primitive variables have been defined, and the system governing Equations (1)–(6) can be formulated in a non-dimensional form.

$$\overline{\omega}=\mathrm{curl}\left(\overline{V}\right),\overline{\gamma}=\mathrm{curl}(\overline{\omega}) \tag{7}$$

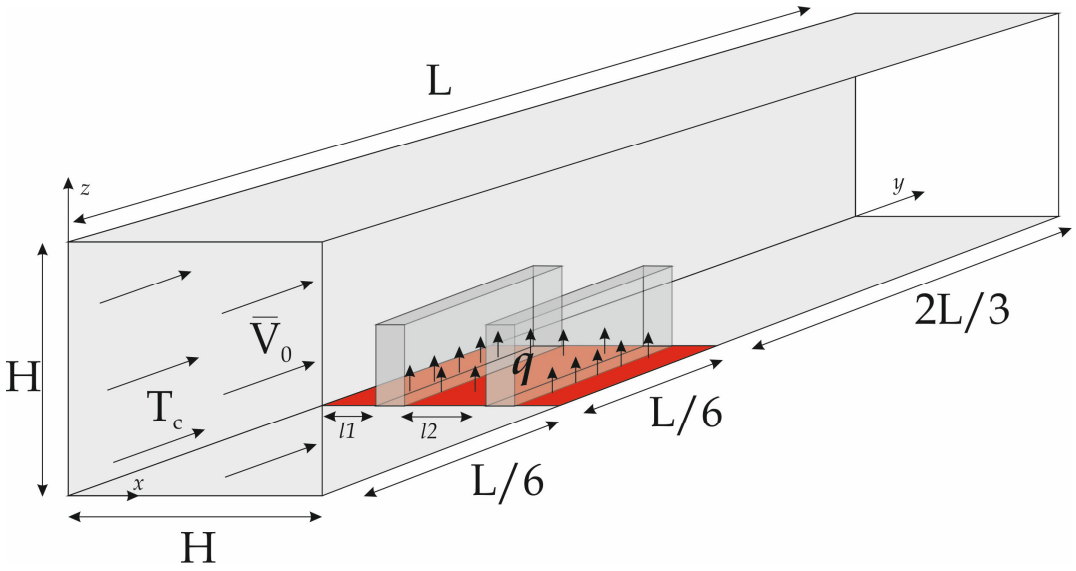

Figure 1. Analyzed geometry with a coordinate system and boundary conditions.

Taking into account the above assumptions, the key differential equations of unsteady conjugate mixed convection inside the channel can be written in dimensionless form. These equations are derived from the conservation laws for mass, momentum, and energy based on the defined non-primitive variables of the vorticity vector and its curl [32,33]:

- For the liquid zone

$$\begin{aligned}&\frac{\partial \Omega_x}{\partial \tau}+U\frac{\partial \Omega_x}{\partial X}+V\frac{\partial \Omega_x}{\partial Y}+W\frac{\partial \Omega_x}{\partial Z}-\Omega_x\frac{\partial U}{\partial X}-\Omega_y\frac{\partial U}{\partial Y}-\Omega_z\frac{\partial U}{\partial Z}\\&=\frac{1}{Re}\left(\frac{\partial^2 \Omega_x}{\partial X^2}+\frac{\partial^2 \Omega_x}{\partial Y^2}+\frac{\partial^2 \Omega_x}{\partial Z^2}\right)+\frac{Ra}{Pr\cdot Re^2}\frac{\partial \Theta}{\partial Y},\end{aligned} \tag{8}$$

$$\begin{aligned}&\frac{\partial \Omega_y}{\partial \tau}+U\frac{\partial \Omega_y}{\partial X}+V\frac{\partial \Omega_y}{\partial Y}+W\frac{\partial \Omega_y}{\partial Z}-\Omega_x\frac{\partial V}{\partial X}-\Omega_y\frac{\partial V}{\partial Y}-\Omega_z\frac{\partial V}{\partial Z}\\&=\frac{1}{Re}\left(\frac{\partial^2 \Omega_y}{\partial X^2}+\frac{\partial^2 \Omega_y}{\partial Y^2}+\frac{\partial^2 \Omega_y}{\partial Z^2}\right)-\frac{Ra}{Pr\cdot Re^2}\frac{\partial \Theta}{\partial X},\end{aligned} \tag{9}$$

$$\begin{array}{l}\frac{\partial \Omega_z}{\partial \tau}+U\frac{\partial \Omega_z}{\partial X}+V\frac{\partial \Omega_z}{\partial Y}+W\frac{\partial \Omega_z}{\partial Z}-\Omega_x\frac{\partial W}{\partial X}-\Omega_y\frac{\partial W}{\partial Y}-\Omega_z\frac{\partial W}{\partial Z}\\ =\frac{1}{Re}\left(\frac{\partial^2 \Omega_z}{\partial X^2}+\frac{\partial^2 \Omega_z}{\partial Y^2}+\frac{\partial^2 \Omega_z}{\partial Z^2}\right),\end{array} \quad (10)$$

$$\begin{array}{l}\Gamma_x=-\nabla^2 U,\\ \Gamma_y=-\nabla^2 V,\ \left\{\overline{\Gamma}=\mathrm{curl}\left(\overline{\Omega}\right)\right\}\\ \Gamma_z=-\nabla^2 W,\end{array} \quad (11)$$

$$\frac{\partial \Theta}{\partial \tau}+U\frac{\partial \Theta}{\partial X}+V\frac{\partial \Theta}{\partial Y}+W\frac{\partial \Theta}{\partial Z}=\frac{1}{Pr\cdot Re}\left(\frac{\partial^2 \Theta}{\partial X^2}+\frac{\partial^2 \Theta}{\partial Y^2}+\frac{\partial^2 \Theta}{\partial Z^2}\right) \quad (12)$$

- Inside the solid ribs:

$$\frac{\partial \Theta}{\partial \tau}=\frac{\alpha_s/\alpha_f}{Pr\cdot Re}\left(\frac{\partial^2 \Theta}{\partial X^2}+\frac{\partial^2 \Theta}{\partial Y^2}+\frac{\partial^2 \Theta}{\partial Z^2}\right) \quad (13)$$

The governing Equations (8)–(13) are supplemented by the following initial and boundary conditions:

Initial conditions are $U = V = W = 0$, $\Omega_x = \Omega_y = \Omega_z = 0$, $\Theta = 0.5$.

Boundary conditions:

- The velocity components on the channel walls are zero $U = V = W = 0$; the walls are considered to be adiabatic $\frac{\partial \Theta}{\partial \overline{n}} = 0$;
- At the flat heater surface the velocity components are also zero $U = V = W = 0$, while for the temperature, we have $\frac{\partial \Theta}{\partial Z} = -1$;
- On the surface of solid fins: $U = V = W = 0$, $\begin{cases} \Theta_s = \Theta_f, \\ \frac{k_s}{k_f}\frac{\partial \Theta_s}{\partial \overline{n}} = \frac{\partial \Theta_f}{\partial \overline{n}}; \end{cases}$
- A liquid with a low temperature ($\Theta = 0$) enters the channel at the inlet port, while for velocity components, we have $U = W = 0$, $V = V_0$;
- At the outlet port, we have $\partial\Theta/\partial Y = 0$, and for the velocity components, one can find $U = W = 0$, $\partial V/\partial Y = 0$.

The formulated boundary-value problem has been solved by the finite difference method on a uniform mesh. To solve the parabolic Equations (8)–(10), (12) and (13), a local one-dimensional Samarskii scheme has been used. This allows the transition from a spatial formulation of the problem to a system of one-dimensional equations with appropriate approximations for the convective and diffusive terms. The Thomas algorithm has solved the resulting system of linear algebraic equations (SLAE). The monotonic Samarskii scheme has been used to approximate the convective terms, while central differences are used to discretize diffusive terms. The system of elliptic Equation (11) has been solved using seven-point difference schemes, which allow moving from a differential form to a system of linear algebraic equations. As a result of the approximation of the partial differential equations by the central differences with a second order of accuracy, the obtained SLAE has been solved by the successive over-relaxation method [34–36].

3. Comparative Study

As an approbation of the developed numerical algorithm, the problem of mixed convection in a channel with heated upper and lower walls with temperature T_w has been chosen. Analysis has been performed for the following values of governing parameters: Reynolds number $Re = 10$, Prandtl number $Pr = 0.7$, the temperature of the working medium at the entrance of the channel is $T_{in} = 20$ °C, and the horizontal component of the velocity vector $u_{in} = 0.01$ m/s. The following non-dimensional temperatures and velocities have been used: $\Theta = \frac{T-T_w}{T_b-T_w}$ and $U = \frac{u}{u_{in}}$. Here, Θ is the dimensionless temperature, U is the dimensionless velocity, T_b is the bulk temperature of the section. Figure 2 shows a comparison between the obtained results and numerical data of Tang et al. [37] for vertical

temperature and velocity profiles. As shown in Figure 2, a good agreement has been obtained, indicating the operability of the developed computational algorithm.

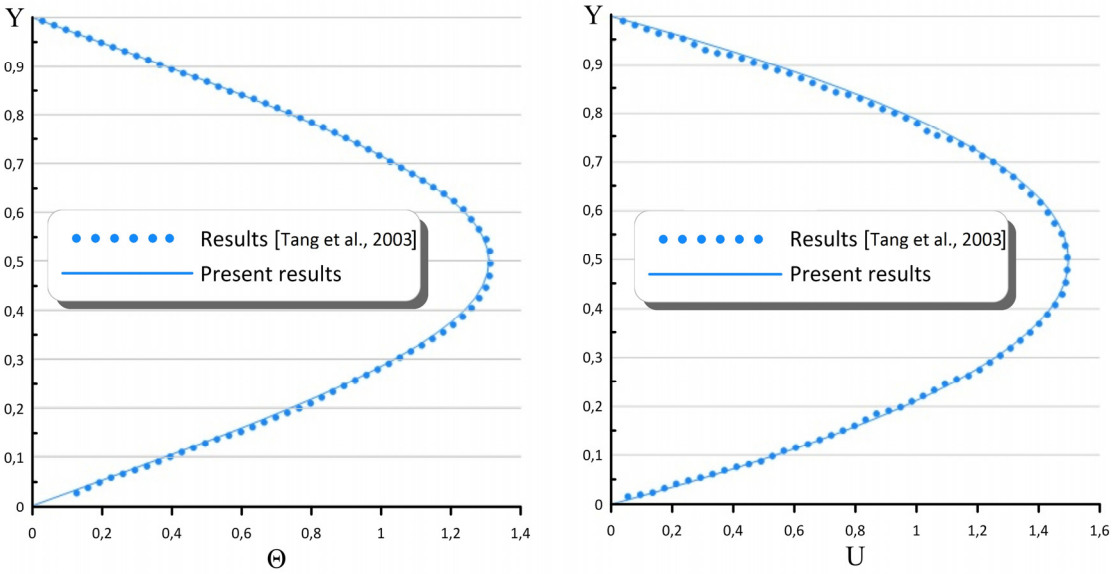

Figure 2. Temperature (Θ) and velocity (U) profiles in comparison with numerical data [37].

Another important verification problem is the mesh sensitivity analysis for the local and integral parameters. Figures 3 and 4 present integral and local characteristics for the problem presented in Figure 1, in the case of Re = 500, aluminum fins, and the position of the fins: $l1/H = 1/5$ ($l2 = l1$). From the data presented in these Figures, it can be concluded that it is possible to use grids of 40 × 120 × 40, 60 × 180 × 60, and 80 × 240 × 80 elements. However, the calculation speed increases up to 2.7 and 6.3 times, respectively, as the dimension increases in these ranges. Therefore, the uniform mesh of 40 × 120 × 40 elements has been chosen as the most optimal grid.

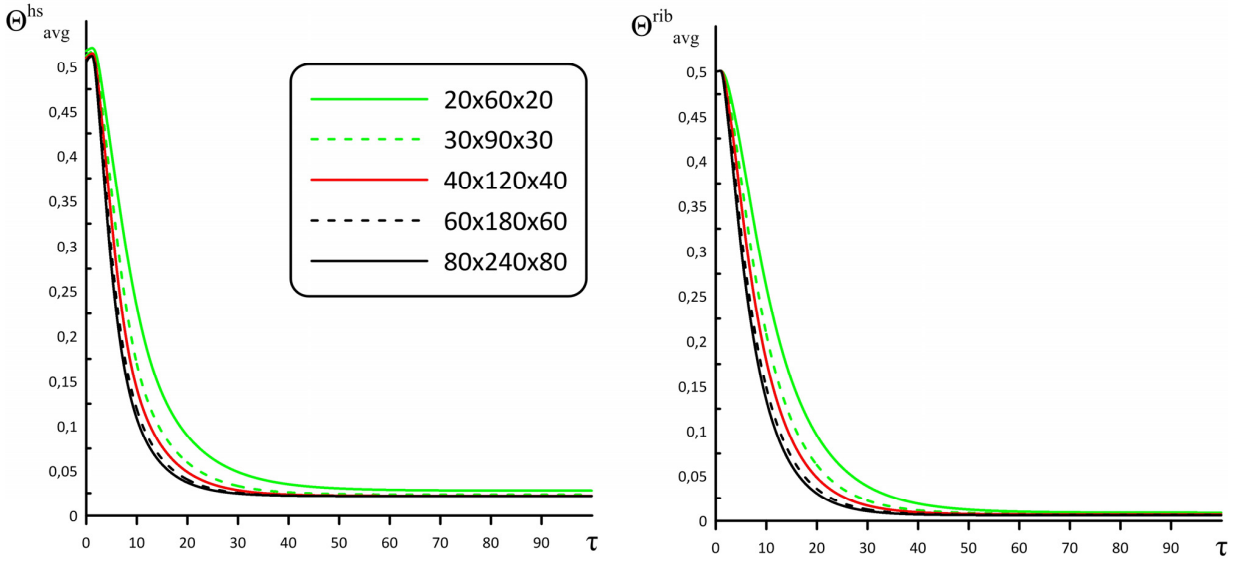

Figure 3. Time dependences for the average heater temperature $\left(\Theta^{hs}_{avg}\right)$ and average fin temperature $\left(\Theta^{rib}_{avg}\right)$ were obtained for different grids.

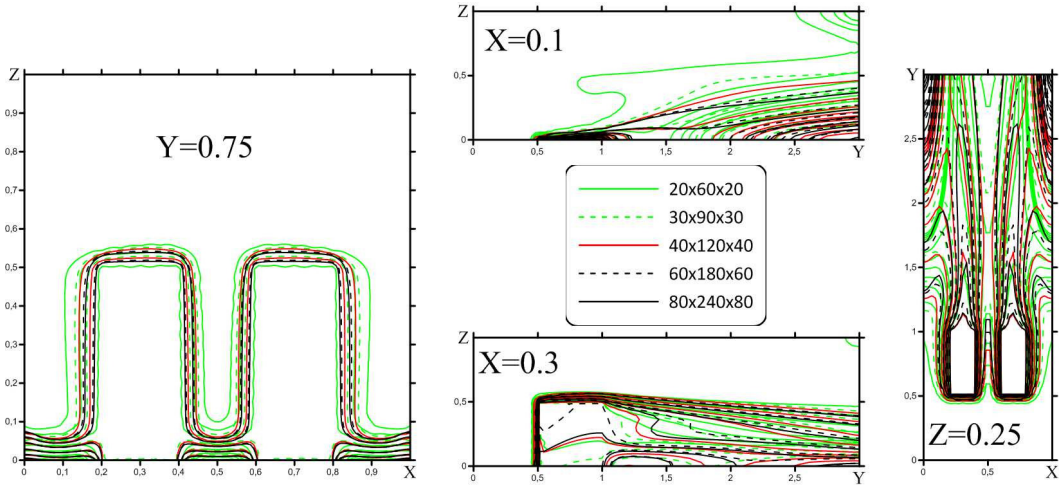

Figure 4. Temperature profiles for different cross-sections were obtained for various grids.

4. Discussion

Numerical calculations have been carried out for the following values of the governing parameters: $200 \leq Re \leq 1000$, $Pr = 6.2$, $Ra = 10^4$, and the solid fin materials are copper (Cu), aluminum (Al), and iron (Fe). Another important parameter in this study is the symmetrical location of the fins on the flat heater. Three positions have been considered, namely, Loc1, Loc2, and Loc3, where Loc1 is for $l1/H = 3/20$ ($l2 = 2 \cdot l1$), Loc2 is for $l1/H = 1/5$ ($l2 = l1$), and Loc3 is for $l1/H = \frac{1}{4}$ ($l2 = 2 \cdot l1/5$). The height of the fins is $h/H = \frac{1}{2}$, and the thickness of the fins is l/H, which is constant and equal to $1/5$. Further, Figures 5–20 present the main results of this research. The positions of the solid fins illustrate a reduction in the non-dimensional distance between these fins from 0.3 for Loc1, 0.2 for Loc2, and 0.1 for Loc3. These symmetrical arrangements for the two-fin system have been selected due to the opportunity to analyze in detail the presence of discrete solid fins and not the asymmetrical interaction between the solid fin surfaces and channel walls.

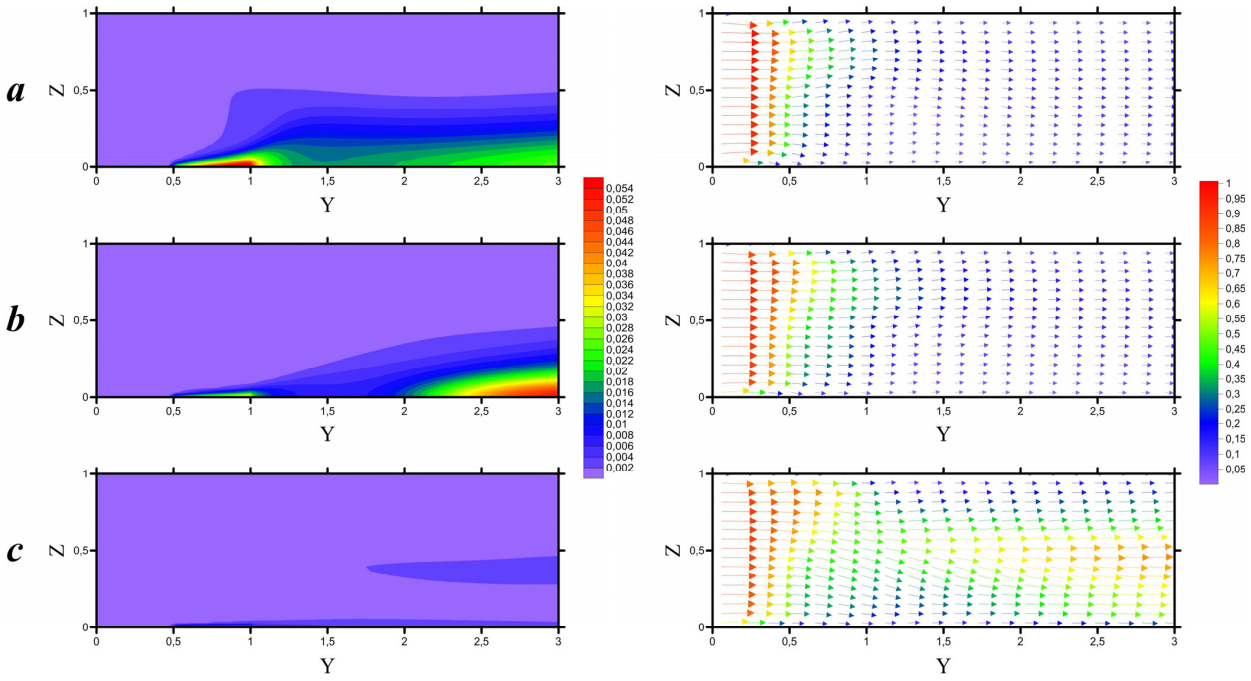

Figure 5. (**a**) $Re = 200$, (**b**) $Re = 500$, and (**c**) $Re = 1000$. The temperature field (left column) and the velocity field (right column) for aluminum fins at different values of the Reynolds number in the cross-section $X = l1/2H$ for the case Loc2.

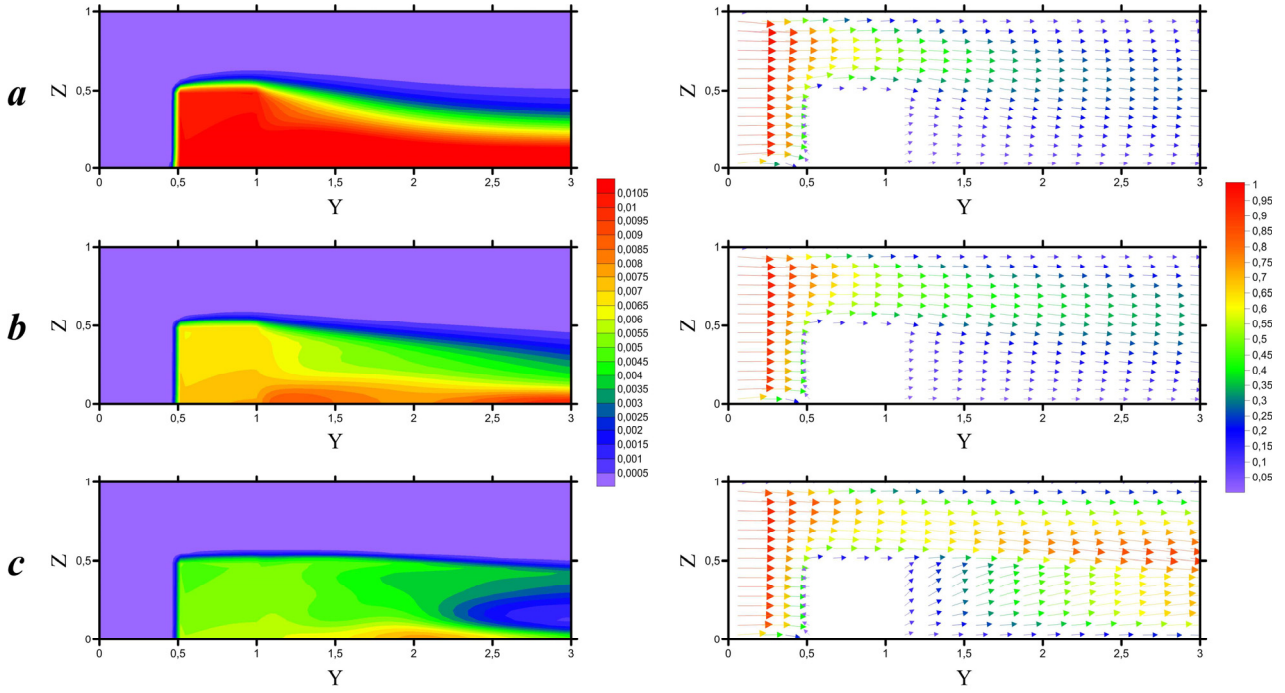

Figure 6. (**a**) Re = 200, (**b**) Re = 500, and (**c**) Re = 1000. The temperature field (left column) and the velocity field (right column) for aluminum fins at different values of the Reynolds number in the cross-section $X = l1/H + l/2H$ for the case Loc2.

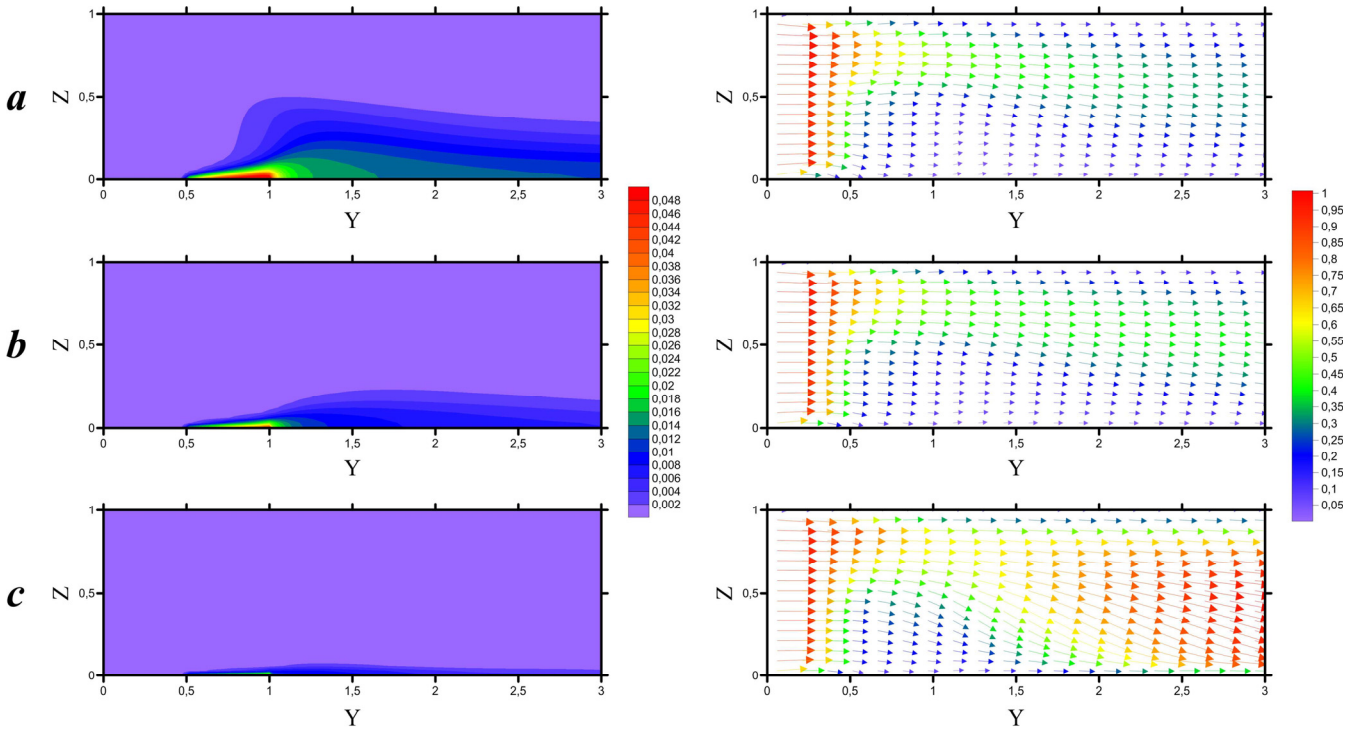

Figure 7. (**a**) Re = 200, (**b**) Re = 500, and (**c**) Re = 1000. The temperature field (left column) and the velocity field (right column) for aluminum fins at different values of the Reynolds number in the cross-section X = 0.5 for the case Loc2.

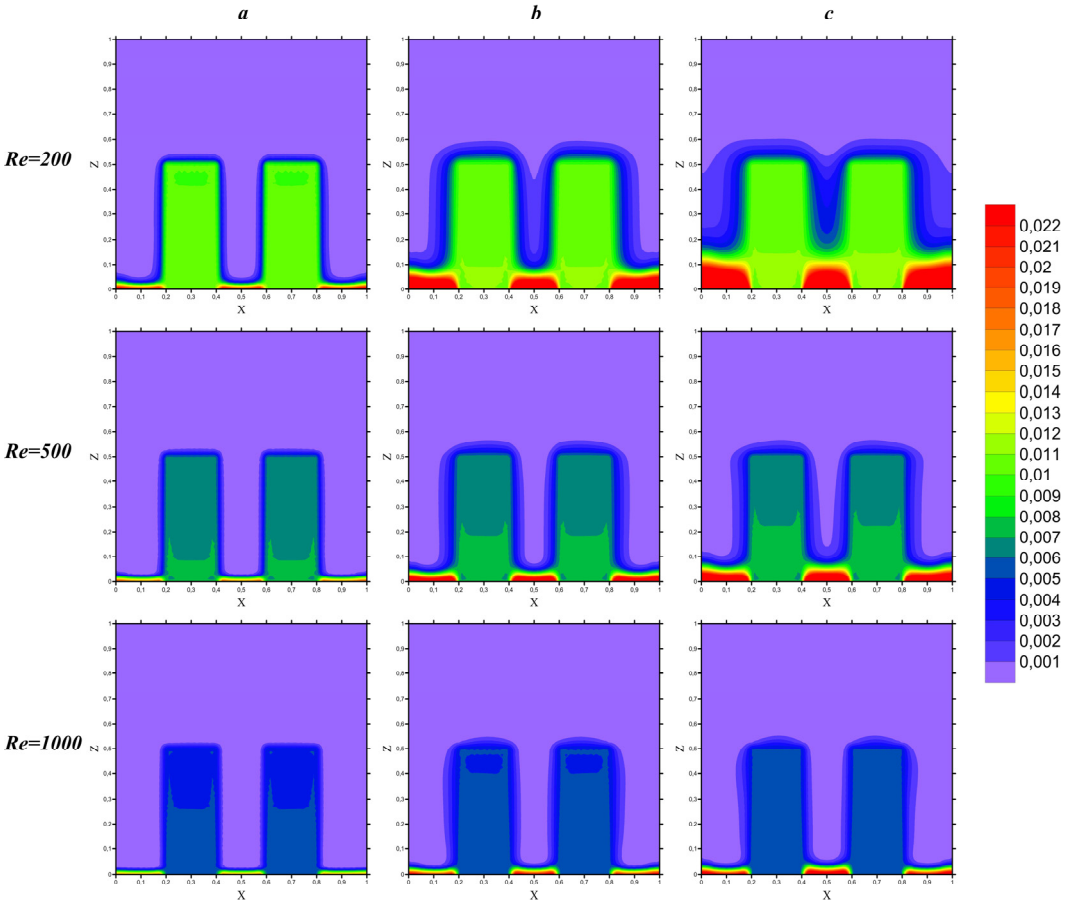

Figure 8. (**a**) $Y = 0.5$, (**b**) $Y = 0.75$, and (**c**) $Y = 1$. The temperature fields for aluminum ribs at different values of the Reynolds number for the case Loc2.

4.1. The Impact of the Reynolds Number

Figures 5–7 show the temperature (left row) and velocity (right row) fields for different cross-sections (X = const) and for various *Re* numbers.

Figure 5 shows that a layer with a thermal plume is formed for a low Reynolds number (Figure 5a), which is practically not carried away by the coolant liquid flow. As a result, a thermal boundary layer is formed above the heater with a slight offset towards the growth of the Y-coordinate. In the case of an increase in the Reynolds number, there is practically no zone of elevated temperature above the energy source. The region of maximum values of the temperature field near the channel outlet at $Re = 500$ is caused by boundary conditions of the second kind on the walls and an initial non-dimensional temperature $\Theta = 0.5$. As a result, the temperature on the surface of these walls has not changed for the considered time interval. The velocity fields in this figure reflect a characteristic decrease in the y-component of the velocity vector when the liquid interacts with the heat sink. However, at $Re = 1000$ (Figure 5c), a noticeable increase in the velocity value in the lower half of the channel is closer to its outlet.

Figure 6 shows similar distributions for cross-sections (X = const) along the center of the fin. It may be noted that a significant decrease in the temperature in the fin with an increase in the velocity of the injected flow in the channel can be found. At $Re = 500$ and $Re = 1000$, a thermal plume is formed behind the heater on the lower surface of the channel due to the thermal insulation properties of the channel walls and the mentioned initial temperature. The flow velocity behind the fin at a low Reynolds number remains low. However, at $Re = 1000$, it can be seen that with the growth of the Y-coordinate, the velocity increases. It is very interesting to highlight the formation of a thermal spot near

the solid fin due to the influence of initial temperature and the formation of complicated recirculation in the form of a toroidal vortex close to the back surface of the fin.

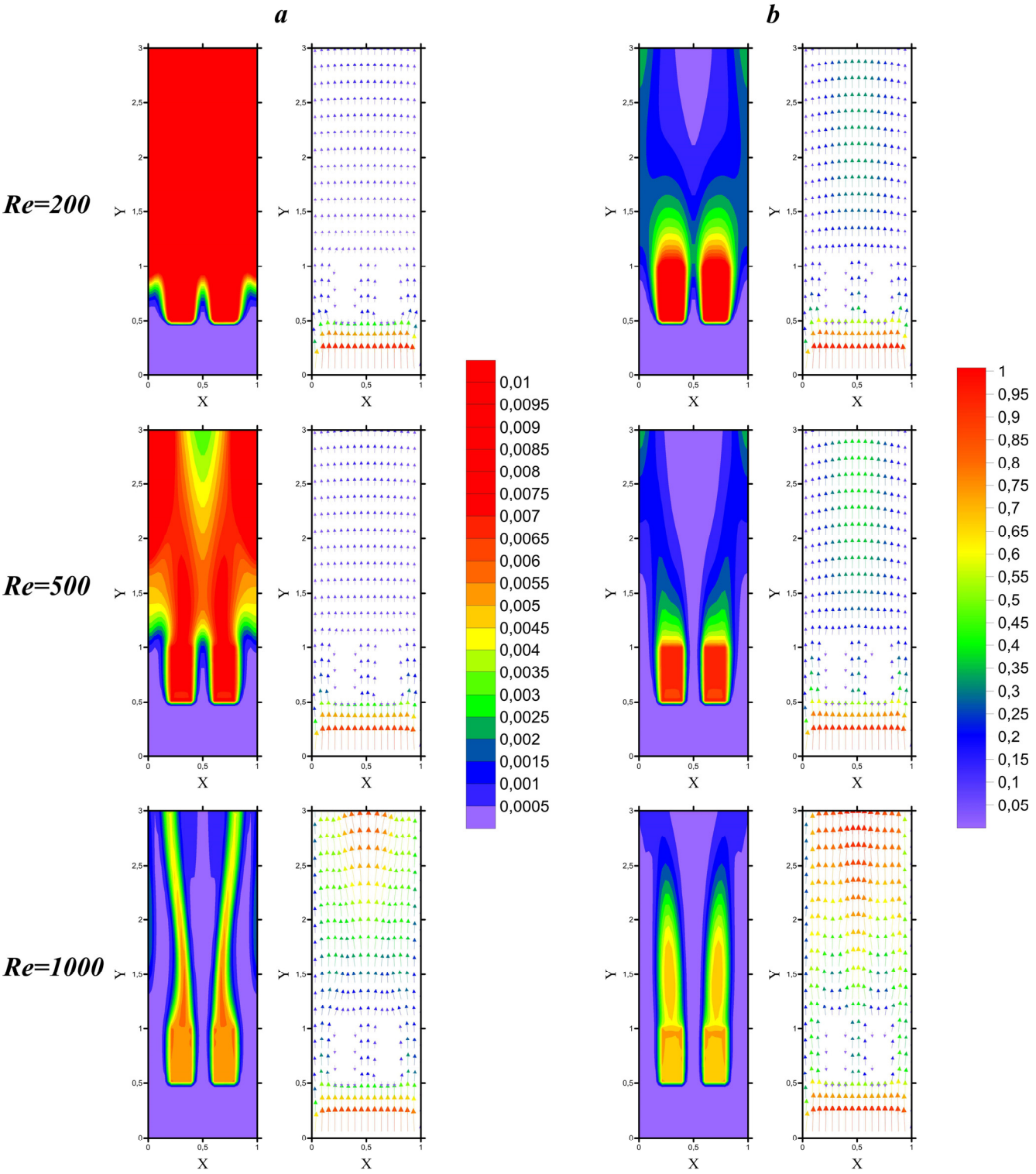

Figure 9. (**a**) $Z = 0.25$ and (**b**) $Z = 0.5$. The temperature fields (left column) and the velocity fields (right column) for aluminum fins at different values of the Reynolds number at Loc2.

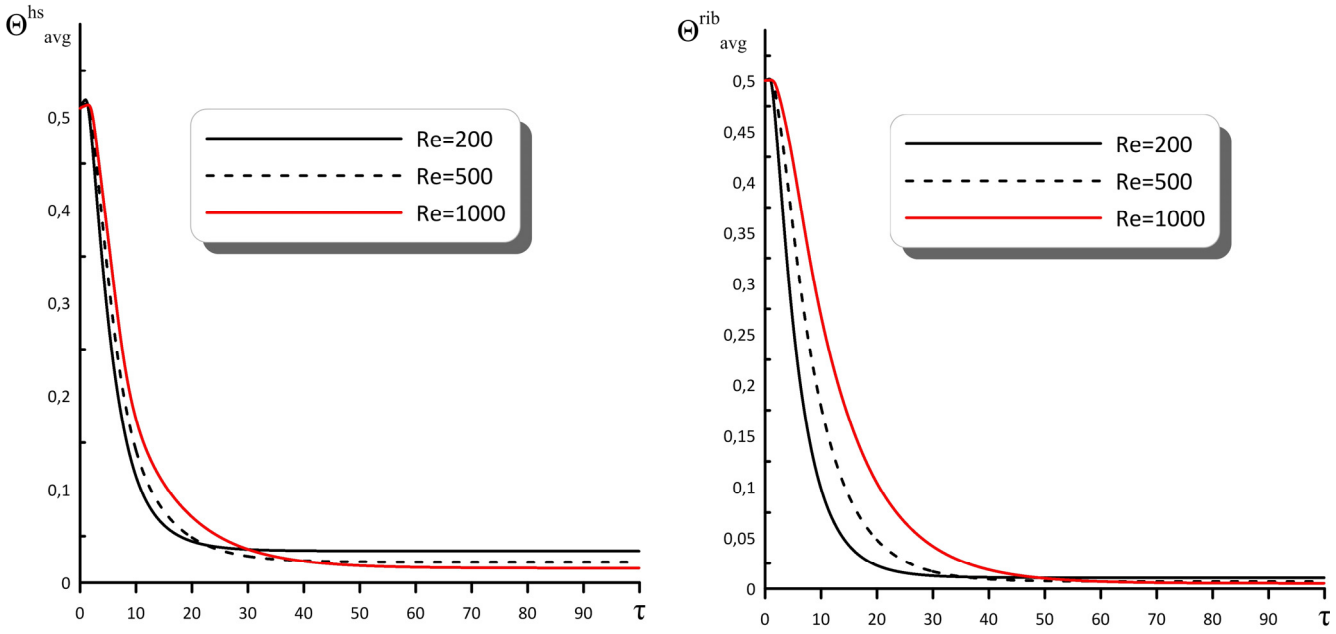

Figure 10. Average heater temperature $\left(\Theta_{avg}^{hs}\right)$ and average fin temperature $\left(\Theta_{avg}^{rib}\right)$ for aluminum fins and case Loc2 at different Reynolds numbers.

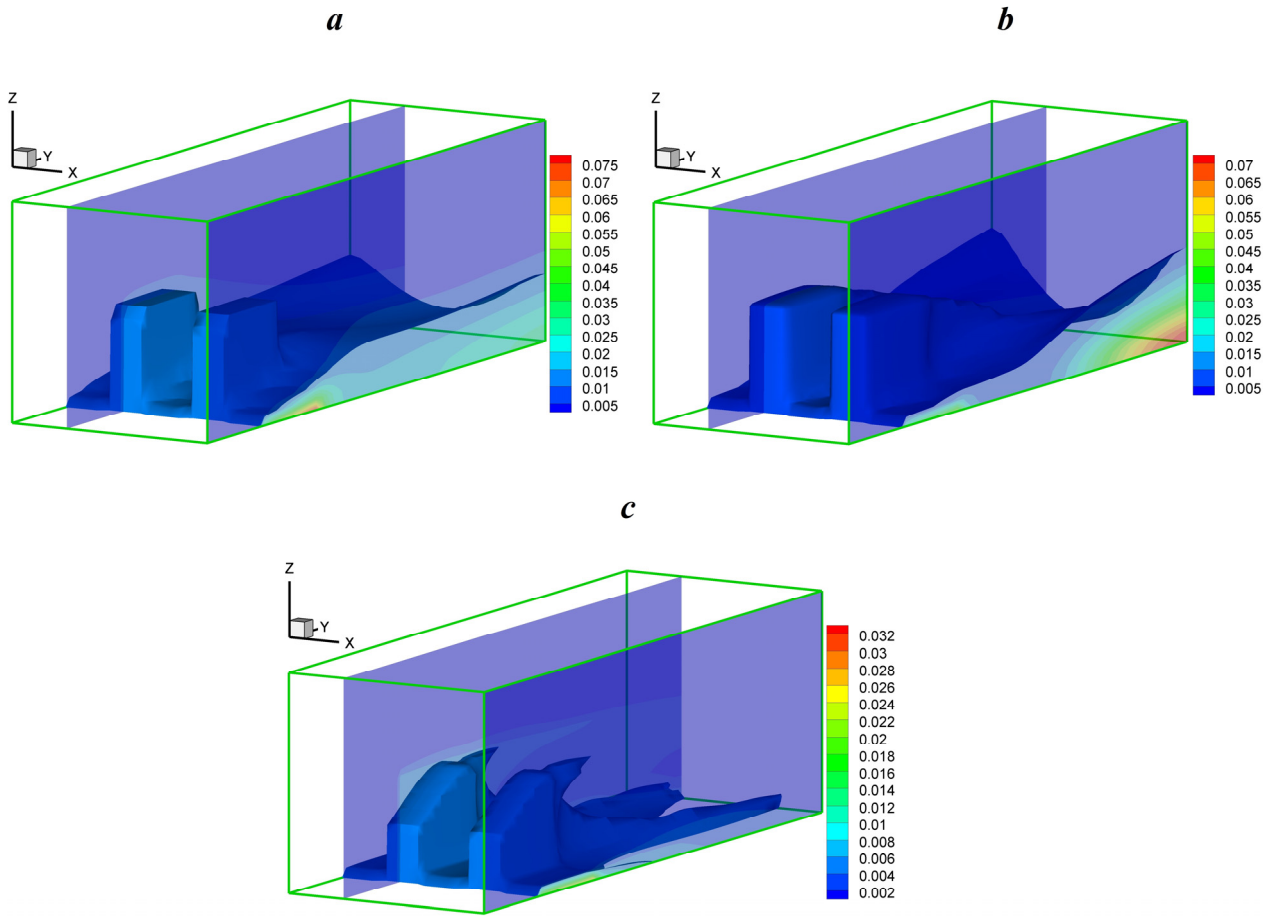

Figure 11. (**a**) *Re* = 200, (**b**) *Re* = 500, and (**c**) *Re* = 1000. Three-dimensional temperature fields for aluminum fins at the case Loc2 for different Reynolds numbers.

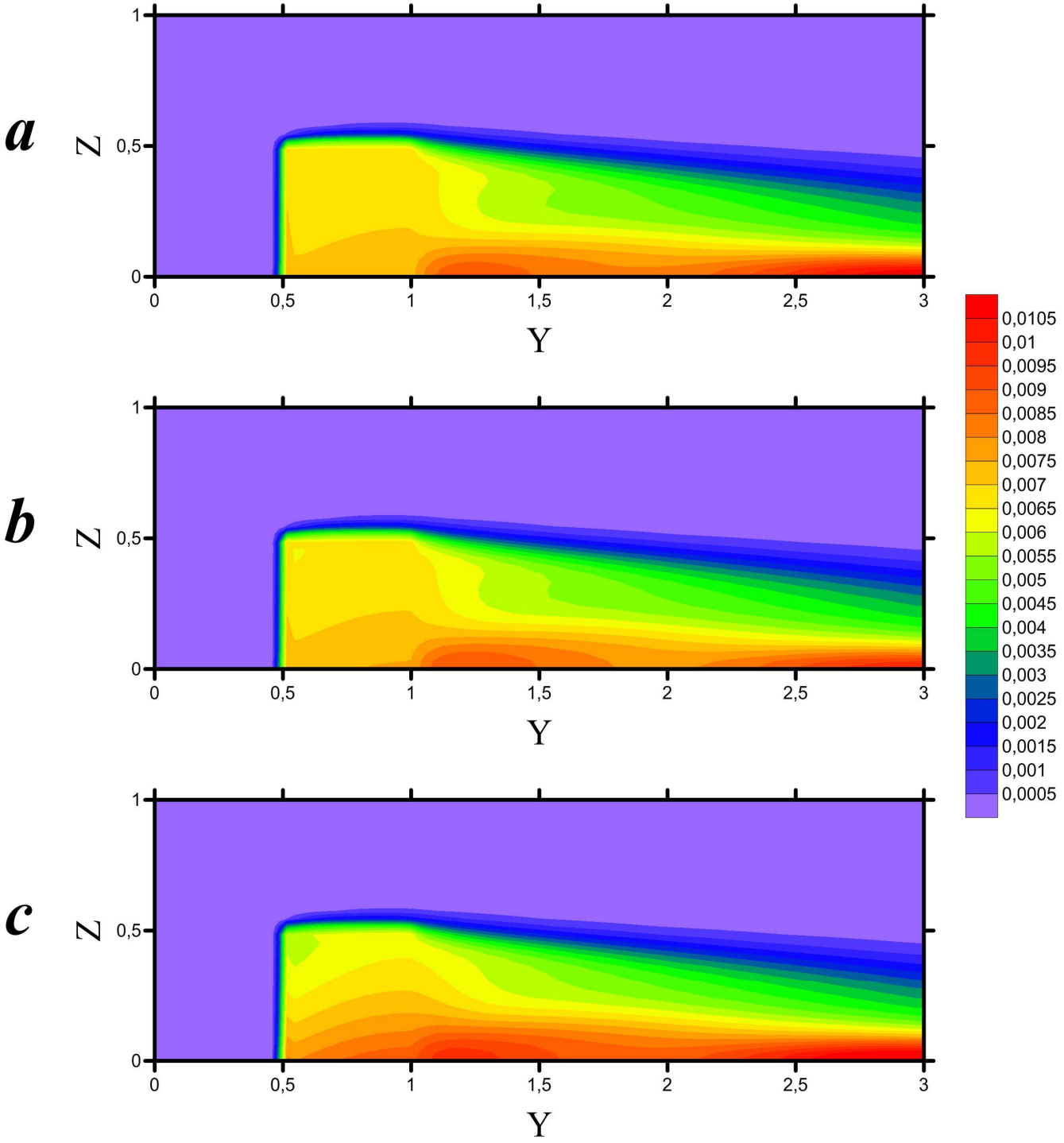

Figure 12. (**a**) Cu, (**b**) Al, and (**c**) Fe. The temperature fields for $Re = 500$ and different materials of fins at $X = l1/H + l/2H$ for Loc2.

Figure 7 demonstrates the temperature and velocity distributions at $X = 1/2$. It can be seen from this figure that when the cooling liquid flow reaches the solid fins, the flow velocity decreases. As a result, a thermal boundary layer is formed above the heater, and at $Re = 1000$, the maximum cooling of the heating element is observed. It should be noted that the zone between the solid fins is more heated compared to the zone after the solid fins and heater. Therefore, for $Re = 200$, one can find a formation of a not so cooled zone between fins, like for high values of the Reynolds number.

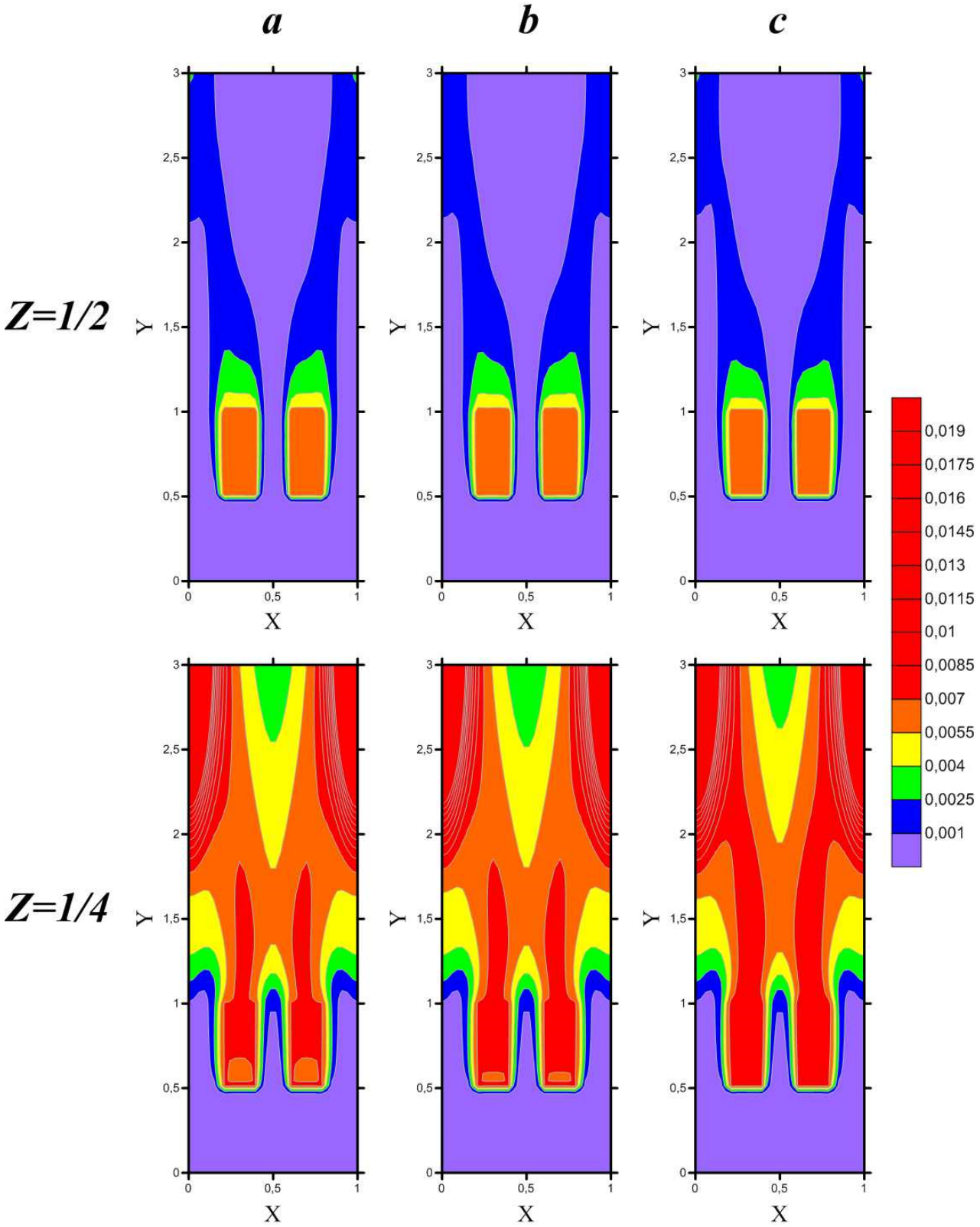

Figure 13. (**a**) Cu, (**b**) Al, and (**c**) Fe. The temperature fields at *Re* = 500 for different fins materials at *Z* = 0.5 and *Z* = 0.25 for the case of Loc2.

Figure 8 shows the temperature distributions for different cross-sections (Y = const). As can be seen from this figure, the heating zone has a minimum temperature in the front part of the fins, where one can find an interaction of the flow with a fin surface. As a result,

the maximum efficiency of heat removal from these surfaces is observed. Moving further along the fins, the temperature of the heating element increases, but the temperature in the ribs remains almost unchanged due to the high thermal conductivity of the fin material. It is also worth noting a significant decrease in temperature in the heater and fins with an increase in the Reynolds number due to essential heat removal from the heated element.

The thermal plume from the solid fins can be seen more clearly in Figure 9 in the cross-section of the cavity for Z = const. At Z = 0.25 and Re = 200, the temperature of the medium near and behind the heater, as well as the source itself, has the same values. As Re increases, the average temperature in the cavity decreases. When Re = 1000, the maximum temperature values are observed in the zone of the back side of the ribs. Figure 9b shows the temperature and velocity fields for Z = 0.5.

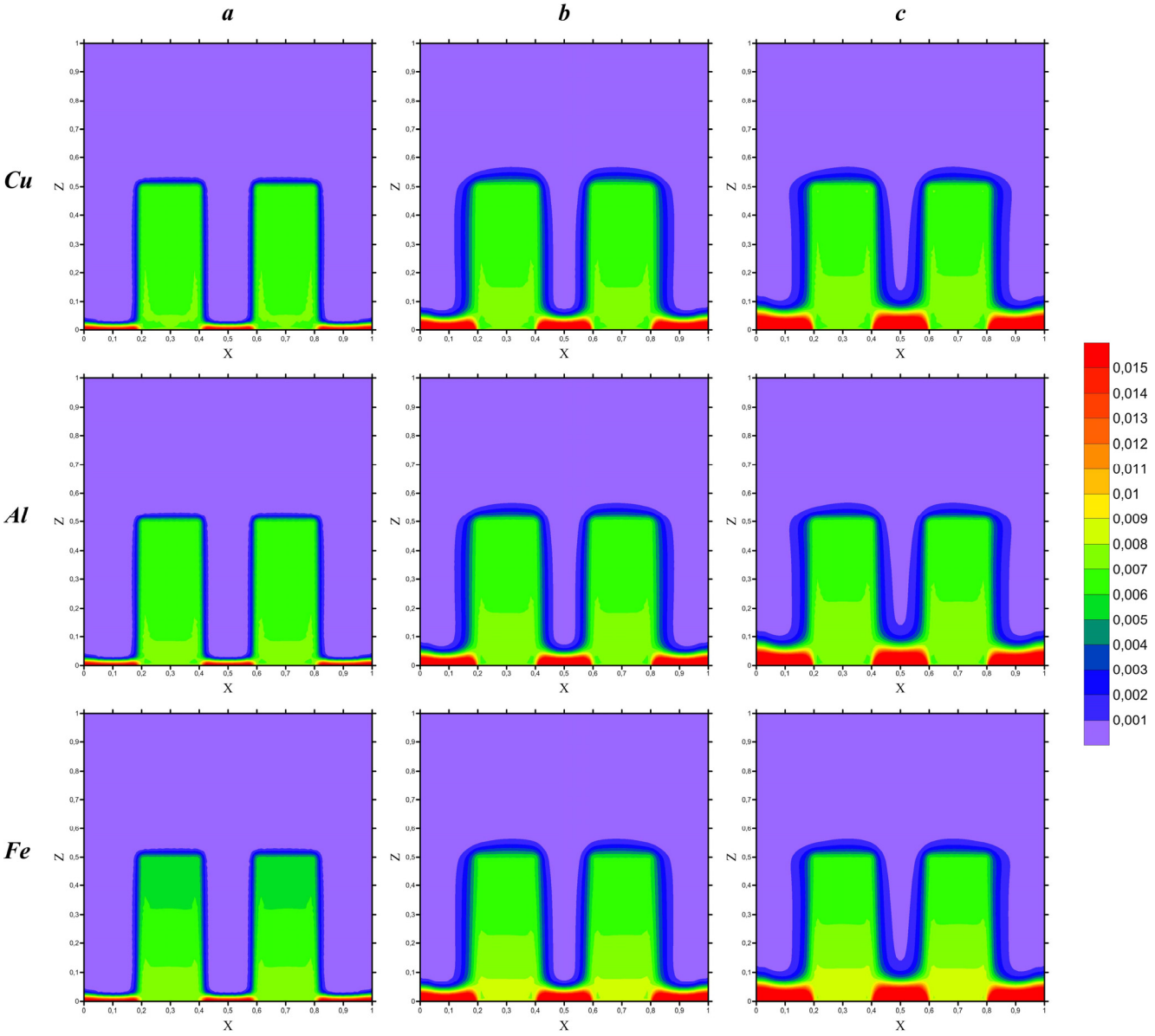

Figure 14. (**a**) Y = 0.5, (**b**) Y = 0.75, and (**c**) Y = 1. Temperature fields for Re = 500 and different fins materials at cross-sections Y = const for the case of Loc2.

Figure 10 shows time profiles of the average temperature inside the heater and solid fins, depending on Re. It can be seen that with an increase in the Reynolds number, the temperature decreases both inside the fins and heater. Therefore, the minimum average temperature for the steady state is equal to 0.00518 within the fin and 0.01552 within the

heater for *Re* = 1000. When the *Re* is reduced to 500, it increases the average temperature within the fin by up to 32% and within the heater by up to 41.7%. Furthermore, for *Re* = 200, one can find the following increments up to 104% and 119%, respectively. In general, low temperatures are observed at the specified parameters due to the choice of water for the cooling liquid, which removes high heat flux. Most often, gases that do not have the same efficiency are used in cooling systems. In such cases, it is necessary to further study the effective parameters for maximum temperature reduction in the heater.

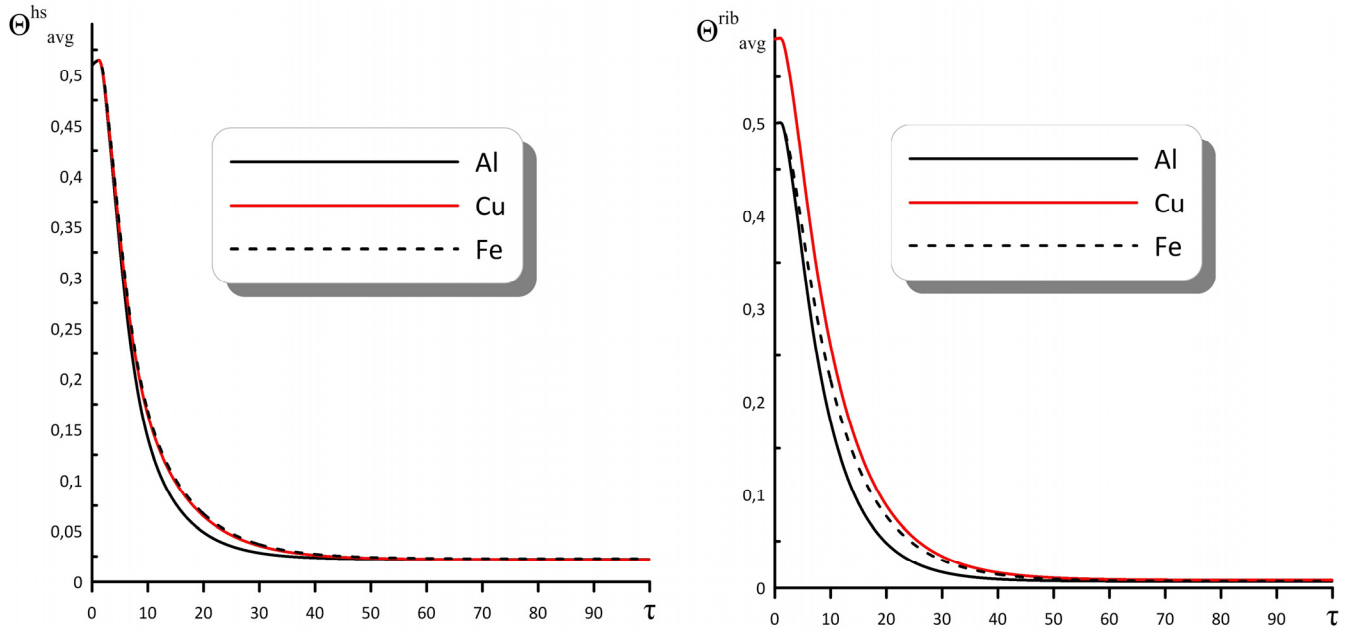

Figure 15. Time profiles of the average heater temperature $\left(\Theta_{avg}^{hs}\right)$ and average fin temperature $\left(\Theta_{avg}^{rib}\right)$ for *Re* = 500 and different fin materials for the case of Loc2.

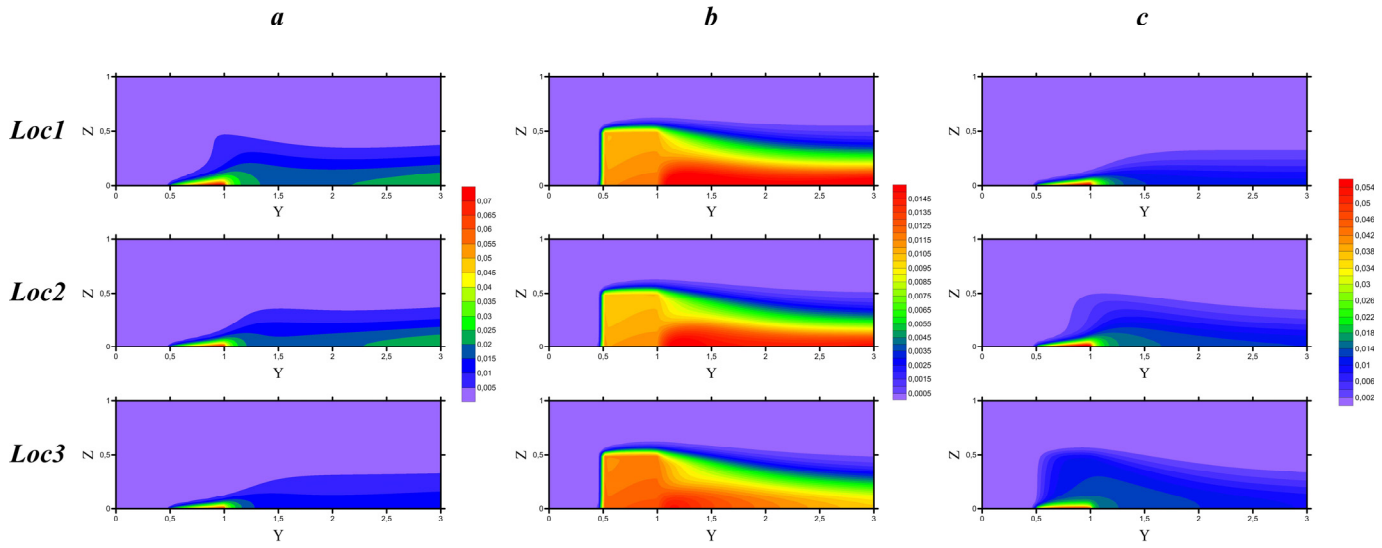

Figure 16. (**a**) $X = 0.5 \cdot l1/H$, (**b**) $X = l1/H + 0.5 \cdot l/H$, and (**c**) $X = l1/H + l/H + 0.5 \cdot l2/H$. Temperature fields for *Re* = 200, aluminum fins, and different fin locations.

Figure 11 shows the temperature field in three-dimensional form. An isosurface is selected at a temperature of Θ = 0.005, which means a zone separating temperature layers. Namely, the area above the specified isosurface corresponds to a lower temperature, while a zone below corresponds to a large one. It can be seen how the shape of this surface changes with an increase in the Reynolds number. A characteristic level appears on the

fins, indicating a decrease in temperature due to the incoming coolant flow to the front boundary. It can also be noted that the area behind the ribs with an increased temperature can be explained by the initial temperature and the less intensive cooling of the side walls.

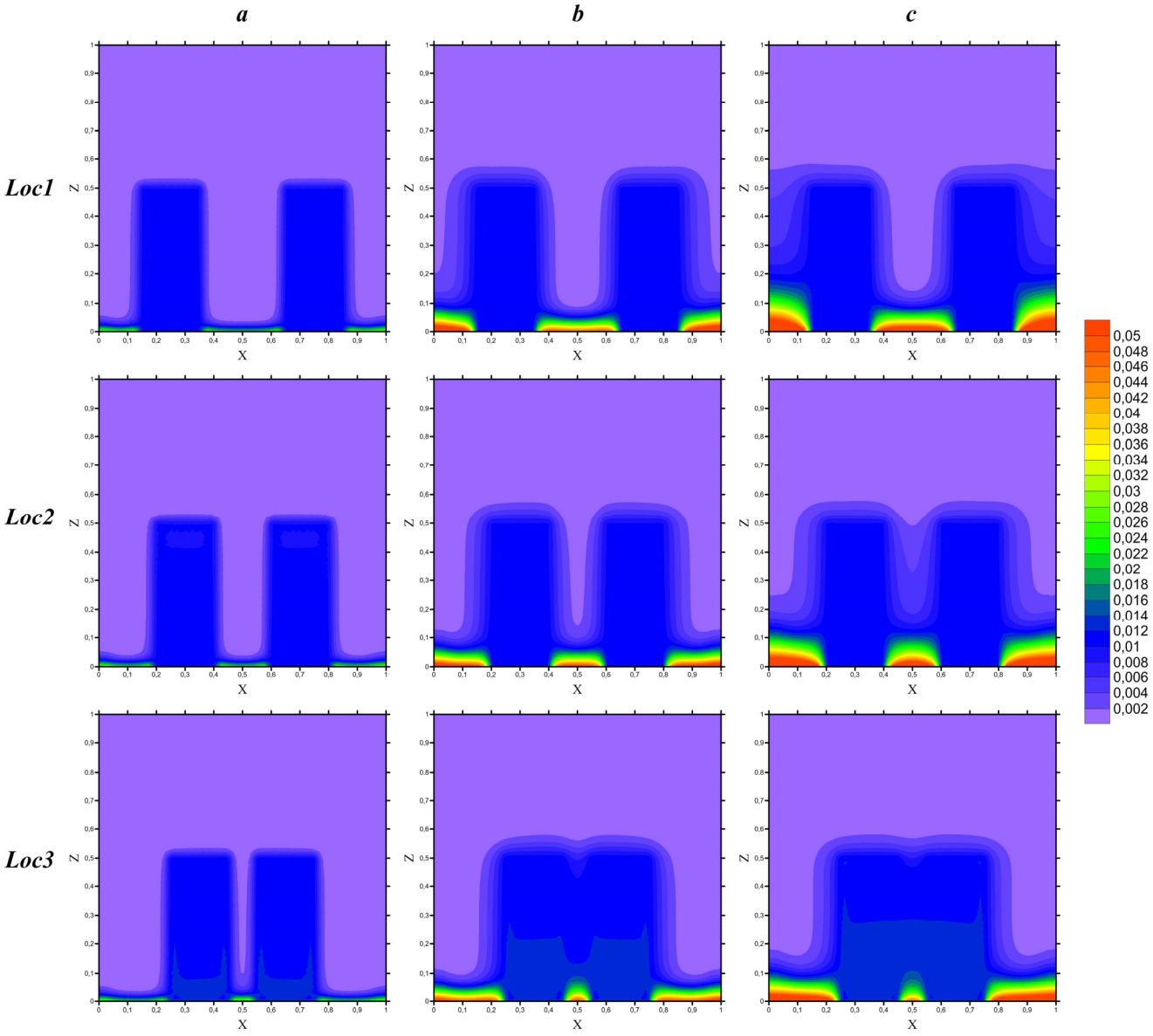

Figure 17. (**a**) $Y = 0.5$, (**b**) $Y = 0.75$, and (**c**) $Y = 1$. Temperature fields for $Re = 200$, aluminum fins, and various fin locations at cross-sections (Y = const).

4.2. The Impact of the Fins Material

Figures 12–16 present the results of the influence of the fin material on flow structures and thermal performance at $Re = 500$ for the case of Loc2.

Figure 12 shows the temperature fields in the cross-section: $X = l1/H + l/2H$. In the case of copper (a) and aluminum (b) fins, the temperature profiles are similar. Only the copper heat sink in the joint zone with the heater has a slightly lower temperature than the aluminum fins due to its higher thermal conductivity. In the case of iron ribs, more obvious temperature isolines are observed, arranged in layers with a characteristic increase in values on the rear right walls of the ribs.

Figure 13 shows the temperature fields for $Z = 0.5$ and $Z = 0.25$. As can be seen from this figure, at $Z = 0.5$, there is practically no difference between the materials of the ribs. This is because at the upper fin surface, the coolant flows around the entire surface, and the

temperature at the time of installation does not differ much for different materials. More significant differences are noticeable in the section $Z = 0.25$. In the copper ribs, areas with a reduced temperature begin to form in the anterior zone, and the lower thermal conductivity of the rib characterizes the formation of the smaller zones.

Figure 14 shows the temperature fields at $Y = 0.5$ (a), $Y = 0.75$ (b), and $Y = 1$ (c) for various fin materials. In the case of a copper rib, the temperature at the front of the wall is almost constant. In contrast, the temperature inhomogeneities are only slightly noticeable at the edge of the rib along the length of the wall for the Z-axis. In the case of aluminum fins, the thermal boundary layer thickness increases near the surface of the heater. In the case of metal ribs, the layered structure of the temperature field is clearly visible. An increase in the temperature of the heater and fins can be found along the fin surface with a Y-coordinate.

Figure 15 shows time dependencies for the average heater and fin temperatures. Almost identical temperatures are observed for the steady state of the heater, and small differences in the average fin temperatures can be found. The differences in the values of the average heater temperatures for different materials do not exceed 3%, and the maximum detected difference in the average temperatures of heat-conducting blocks made of copper and iron is less than 15%.

4.3. The Impact of Fins Location

Figures 16–20 show the velocity, temperature fields, and time profiles of the average temperatures depending on the aluminum fin location at $Re = 200$.

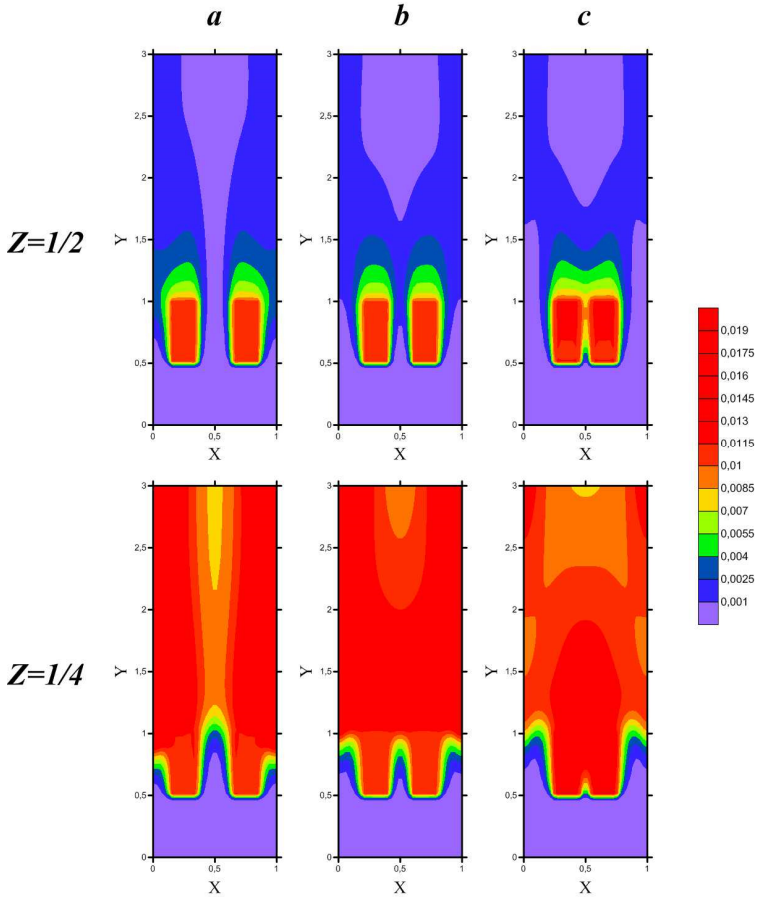

Figure 18. (**a**) Loc1, (**b**) Loc2, and (**c**) Loc3. Temperature fields for $Re = 200$, aluminum fins, and different fin locations at various Z cross-sections.

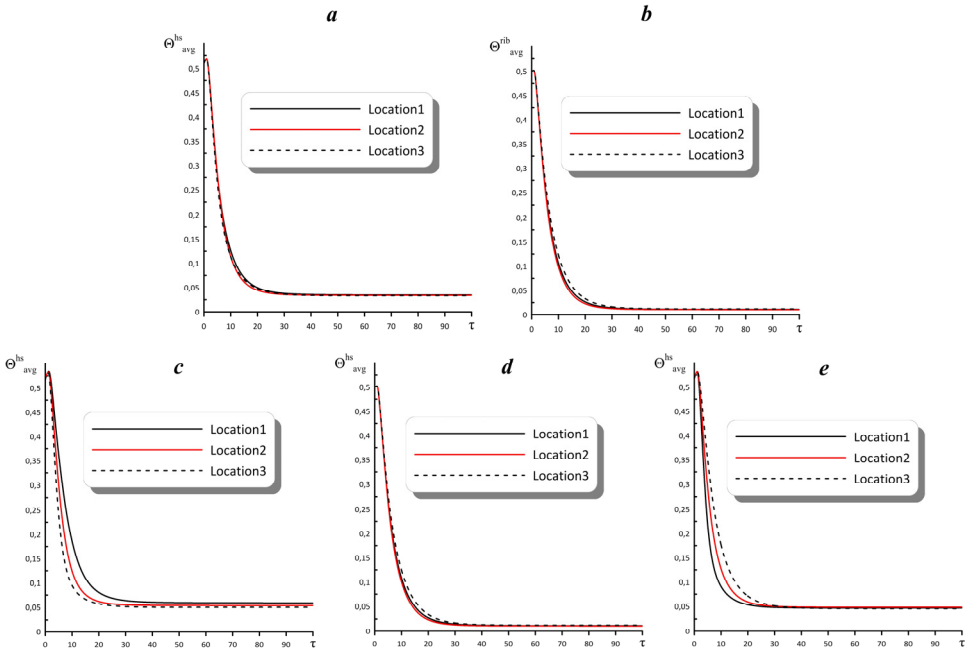

Figure 19. (**a**) Θ_{avg} within the heat source; (**b**) Θ_{avg} within the fin; (**c**) Θ_{avg} within the heater in zone *l*1/*H*; (**d**) Θ_{avg} within the heater under the fin; (**e**) Θ_{avg} within the heater in zone between two heat-conducting blocks time profiles of average heater $\left(\Theta_{avg}^{hs}\right)$ and fin $\left(\Theta_{avg}^{rib}\right)$ temperatures for *Re* = 200 and aluminum fins.

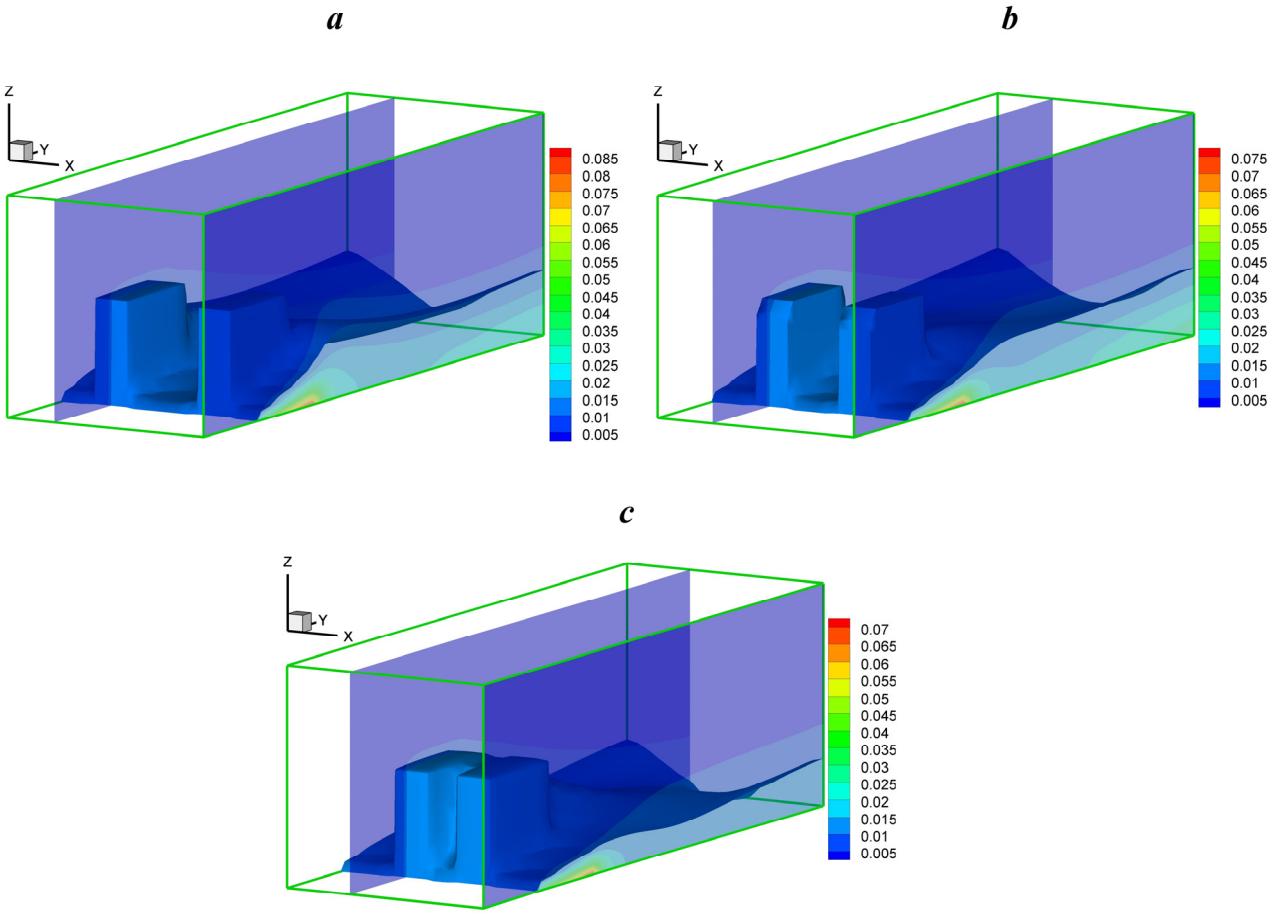

Figure 20. (**a**) Loc1, (**b**) Loc2, and (**c**) Loc3. Three-dimensional temperature fields for aluminum fins and *Re* = 200.

Figure 16 shows the temperature fields for different fin positions and various cross-sections. When the fins are close to the wall (Loc1), the flow velocity in this small interval decreases, and the temperature increases. In the case of increasing the distance of the fins from the wall, the velocity of the fluid increases. As a result, the temperature drops. The opposite effect is observed in the area between two fins, namely, with a decrease in $l1/H$, $l2/H$ increases. The results are more interesting directly in the sections along the fins, where, with the maximum convergence of the fins, the temperature within the fins begins to increase due to a decrease in the flow rate between them. As a result, the heat transfer from the inner surfaces of the ribs worsens, and the temperature in them begins to rise. What can have a negative effect in the future? It is the overheating of the energy source. In this case, the best indicators are the average location of the edges. In support of this analysis, Figures 17 and 18 show an increase in temperature when the two heaters come close together. Figure 18 shows that the zones of maximum temperatures at Loc1 and Loc2 are placed behind the heat-conducting blocks, which is due to the drift of the heated medium by the flow. In the case of Loc3, the maximum temperatures are observed in the zone under the ribs, which should cool.

Figure 19 shows the time profiles of the average heater and fin temperatures (a and b, respectively). At a steady state, the effect of the position is insignificant. The maximum average heater temperature corresponds to the position of Loc1, which is 0.03478. Additionally, the minimum temperature is observed at Loc3, which is 0.033154. It is worth paying attention to the components of this figure. The most valuable results due to the purpose of this study are the control and reduction in the general heater temperature and the area under the ribs in particular. Figure 19d shows profiles of this temperature. The best cooling of the energy source corresponds to Loc2, while in Loc3, an increase of 12% is observed.

Figure 20 shows the spatial temperature distributions, showing the region's growth with high temperatures behind the fins at their maximum convergence. The bevels of the end sides are observed only at the Loc2 position, which indicates its efficiency prevailing over the rest of the locations.

5. Conclusions

In this paper, a numerical study was performed of the unsteady laminar conjugate mixed convection of water in a spatial channel of square cross-section with a local flat source of constant heat flux and a symmetrical solid two-fin system placed on its surface. The main subject of this study is the analysis of the influence of the inlet flow velocity, fin material thermophysical properties, and fin location on the heat transfer performance. Additionally, this study aims to investigate how these parameters can be utilized to control the heat transfer process. It has been shown that with an increase in the Reynolds number, the temperature in both the heating element and the fins decreases significantly. Thus, with an increase in the Reynolds number from 200 to 1000, the average heater temperature decreases by up to 119%, while for the fins, one can find a reduction of up to 104%. An analysis of the influence of the solid fin material on the heat transfer performance and flow structures has been carried out. The significant differences in the average heater and fin temperatures have not been achieved at a steady state, which can be explained by the high values of the thermal conductivity of the considered aluminum and copper fins. The difference in the values of average heater temperatures between the two cases, namely, with copper and iron fins, is 3%. In contrast, the maximum difference in the average fin temperature is 15% for iron and copper fins. Also, the influence of the symmetrical fin location has been evaluated. It has been found that the most optimal position is Loc2, where $l1/H = 0.2$ and $l2 = l1$. When the solid fins are located near each other, the temperature in the zone below them can increase by up to 12%, leading to overheating of the energy source.

It is well known that analyzing entropy generation for engineering systems is very important. Therefore, further analysis within the considered scope can be related to the entropy generation analysis for the considered cooling systems with solid fins, considering

the symmetrical location and asymmetrical position of the fins. At the same time, including porous fins is more useful and interesting, and such a study will also be performed.

Author Contributions: Conceptualization N.S.G. and M.A.S.; methodology N.S.G. and M.A.S.; software, N.S.G. and M.A.S.; validation, N.S.G. and M.A.S.; investigation, N.S.G.; writing—original draft preparation, N.S.G. and M.A.S.; writing—review and editing, N.S.G. and M.A.S.; visualization, N.S.G.; supervision, M.A.S. All authors have read and agreed to the published version of the manuscript.

Funding: This work was supported by the Russian Science Foundation (grant No. 22-79-00291).

Data Availability Statement: The data presented in this study are available on request from the corresponding author.

Conflicts of Interest: The authors declare no conflict of interest.

Nomenclature

g	Gravity acceleration (m s^{-2})
H	Height and width of cavity (m)
k_f	Thermal conductivity of fluid (W m^{-1} K^{-1})
k_s	Thermal conductivity of solid fins (W m^{-1} K^{-1})
L	Length of cavity (m)
p	Pressure (Pa)
Pr	Prandtl number
Ra	Rayleigh number
Re	Reynolds number
T	Temperature (K)
T_0	Ambient temperature (K)
t	Time (s)
U, V, W	Dimensionless velocity components
u, v, w	Velocity components (m s^{-1})
X, Y, Z	Dimensionless coordinates
x, y, z	Cartesian coordinates (m)
α_f	Thermal diffusivity of fluid (m^2 s^{-1})
α_s	Thermal diffusivity of solid fins (m^2 s^{-1})
β	Thermal expansion coefficient (K^{-1})
Γ	Dimensionless vorticity curl
γ	Vorticity curl (m^{-1} s^{-1})
Θ	Dimensionless temperature
ν	Kinematic viscosity (m^2 s^{-1})
ρ	Fluid density (kg m^{-3})
τ	Dimensionless time
Ω	Dimensionless vorticity
ω	Vorticity (s^{-1})

References

1. Incropera, F.P.; Dewitt, D.P.; Bergman, T.L.; Lavine, A.S. *Fundamentals of Heat and Mass Transfer*, 6th ed.; John Wiley & Sons: Hoboken, NJ, USA, 2007; p. 1076.
2. Hagen, G. Ueber die Bewegung des Wassers in engen cylindrischen Röhren. *Ann. Der Phys. Und. Chem.* **1839**, *122*, 423–442. [CrossRef]
3. Poiseuille, J. Recherches expérimentales sur le mouvement des liquides dans les tubes de très petits diamètres. *Mémoires Présentés Par Divers. Savants L'académie R. Sci. L'institut Fr.* **1846**, *9*, 433–544.
4. Sáchica, D.; Treviño, C.; Martínez-Suástegui, L. Numerical study of magnetohydrodynamic mixed convection and entropy generation of Al_2O_3-water nanofluid in a channel with two facing cavities with discrete heating. *Int. J. Heat Fluid Flow* **2020**, *86*, 108713. [CrossRef]
5. Qureshi, M.A.; Hussain, S.; Sadiq, M.A. Numerical simulations of MHD mixed convection of hybrid nanofluid flow in a horizontal channel with cavity: Impact on heat transfer and hydrodynamic forces. *Case Stud. Therm. Eng.* **2021**, *27*, 101321. [CrossRef]
6. Huang, P.C.; Yang, C.F.; Hwang, J.J.; Chiu, M.T. Enhancement of forced-convection cooling of multiple heated blocks in a channel using porous covers. *Int. J. Heat Mass Transf.* **2005**, *48*, 647–664. [CrossRef]
7. Premachandran, B.; Balaji, C. Conjugate mixed convection with surface radiation from a horizontal channel with protruding heat sources. *Int. J. Heat Mass Transf.* **2006**, *49*, 3568–3582. [CrossRef]

8. Ali, M.M.; Akhter, R.; Miah, M.M. Hydromagnetic mixed convective flow in a horizontal channel equipped with Cu-water nanofluid and alternated baffles. *Int. J. Thermofluids* **2021**, *12*, 100118. [CrossRef]
9. Yerramalle, C.; Premachandran, B.; Talukdar, P. Mixed convection from a heat source in a channel with a porous insert: A numerical analysis based on local thermal non-equilibrium model. *Therm. Sci. Eng. Prog.* **2021**, *25*, 101010. [CrossRef]
10. Mandal, S.K.; Deb, A.; Sen, D. Mixed convective heat transfer with surface radiation in a rectangular channel with heat sources in presence of heat spreader. *Therm. Sci. Eng. Prog.* **2019**, *14*, 100423. [CrossRef]
11. Yang, M.-H.; Yeh, R.-H.; Hwang, J.-J. Mixed convective cooling of a fin in a channel. *Int. J. Heat Mass Transf.* **2010**, *53*, 760–771. [CrossRef]
12. Boutina, L.; Bessaïh, R. Numerical simulation of mixed convection air-cooling of electronic components mounted in an inclined channel. *Appl. Therm. Eng.* **2011**, *31*, 2052–2062. [CrossRef]
13. Pishkar, I.; Ghasemi, B. Cooling enhancement of two fins in a horizontal channel by nanofluid mixed convection. *Int. J. Therm. Sci.* **2012**, *59*, 141–151. [CrossRef]
14. Nouraei, S.; Anvari, A.; Abed, A.M.; Akbari, O.A.; Montazerifar, F.; Baghaei, S.; Fatholahi, M. Heat transfer and entropy analysis for nanofluid flow in a semi-circular open cavity under mixed convection. *Alex. Eng.* **2023**, *64*, 309–334. [CrossRef]
15. Umavathi, J.C.; Sheremet, M.A. Mixed convection flow of an electrically conducting fluid in a vertical channel using Robin boundary conditions with heat source/sink. *Eur. J. Mech. B/Fluids* **2016**, *55*, 132–145. [CrossRef]
16. Biswas, N.; Mahapatra, P.S.; Manna, N.K. Thermal management of heating element in a ventilated enclosure. *Int. Commun. Heat Mass Transf.* **2015**, *66*, 84–92. [CrossRef]
17. Biswas, N.; Mahapatra, P.S.; Manna, N.K. Mixed convection heat transfer in a grooved channel with injection. *Numer. Heat Transf. Part A Appl. Int. J. Comput. Methodol.* **2015**, *68*, 663–685. [CrossRef]
18. Biswas, N.; Mahapatra, P.S.; Manna, N.K. Buoyancy-driven fluid and energy flow in protruded heater enclosure. *Meccanica* **2016**, *561*, 2159–2184. [CrossRef]
19. Biswas, N.; Mahapatra, P.S.; Manna, N.K. Enhanced thermal energy transport using adiabatic block inside lid-driven cavity. *Int. J. Heat Mass Transf.* **2016**, *100*, 407–427. [CrossRef]
20. Biswas, N.; Manna, N.K.; Datta, P.; Mahapatra, P.S. Analysis of heat transfer and pumping power for bottom-heated porous cavity saturated with Cu-water nanofluid. *Powder Technol.* **2018**, *326*, 356–369. [CrossRef]
21. Biswas, N.; Manna, N.K.; Datta, A.; Mandal, D.K.; Denim, A.C. Role of aspiration to enhance MHD convection in protruded heater cavity. *Prog. Comput. Fluid Dyn. Int. J.* **2020**, *20*, 363–378. [CrossRef]
22. Chakravarty, A.; Biswas, N.; Ghosh, K.; Manna, N.K.; Mukhopadhyay, A.; Sen, S. Impact of side injection on heat removal from truncated conical heat-generating porous bed: Thermal non-equilibrium approach. *J. Therm. Anal. Calorim.* **2021**, *143*, 3741–3760. [CrossRef]
23. Kamath, P.M.; Balaji, C.; Venkateshan, S.P. Experimental investigation of flow assisted mixed convection in high porosity foams in vertical channels. *Int. J. Heat Mass Transf.* **2011**, *54*, 5231–5241. [CrossRef]
24. Mandev, E.; Manay, E. Effects of surface roughness in multiple microchannels on mixed convective heat transfer. *Appl. Therm. Eng.* **2022**, *217*, 119102. [CrossRef]
25. Dogan, A.; Sivrioglu, M.; Baskaya, S. Experimental investigation of mixed convection heat transfer in a rectangular channel with discrete heat sources at the top and at the bottom. *Int. Commun. Heat Mass Transf.* **2005**, *32*, 1244–1252. [CrossRef]
26. Durgam, S.; Venkateshan, S.P.; Sundararajan, T. Experimental and numerical investigations on optimal distribution of heat source array under natural and forced convection in a horizontal channel. *Int. J. Therm. Sci.* **2017**, *115*, 125–138. [CrossRef]
27. Boulemtafes-Boukadouma, A.; Abid, C.; Benzaoui, A. 3D Numerical study of the effect of aspect ratio on mixed convection air flow in upward solar air heater. *Int. J. Heat Fluid Flow* **2020**, *84*, 108570. [CrossRef]
28. Rhodes, T.J.; Pulugundla, G.; Smolentsev, S.; Abdou, M. 3D modelling of MHD mixed convection flow in a vertical duct with transverse magnetic field and volumetric or surface heating. *Fusion Eng. Des.* **2020**, *160*, 111834. [CrossRef]
29. Danane, F.; Boudiaf, A.; Mahfoud, O.; Ouyahia, S.-E.; Labsi, N.; Benkahla, Y.-K. Effect of backward facing step shape on 3D mixed convection of Bingham fluid. *Int. J. Therm. Sci.* **2020**, *147*, 106116. [CrossRef]
30. Jiang, X.; Hatami, M.; Abderrahmane, A.; Younis, O.; Makhdoum, B.M.; Guedri, K. Mixed convection heat transfer and entropy generation of MHD hybrid nanofluid in a cubic porous cavity with wavy wall and rotating cylinders. *Appl. Therm. Eng.* **2023**, *226*, 120302. [CrossRef]
31. Qu, Y.; Wang, L.; Lin, X.; Chen, H.; Zhang, S.; Ling, H.; Bai, Y. Mixed convective heat transfer characteristics and mechanisms in structured packed beds. *Particuology* **2023**, *82*, 122–133. [CrossRef]
32. Gibanov, N.S.; Sheremet, M.A. Unsteady natural convection in a cubical cavity with a triangular heat source. *Int. J. Numer. Methods Heat Fluid Flow* **2017**, *27*, 1795–1813. [CrossRef]
33. Gibanov, N.S.; Sheremet, M.A. Natural convection in a cubical cavity with different heat source configurations. *Therm. Sci. Eng. Prog.* **2018**, *7*, 138–145. [CrossRef]
34. Bondareva, N.S.; Sheremet, M.A. 3D natural convection melting in a cubical cavity with a heat source. *Int. J. Therm. Sci.* **2017**, *115*, 43–53. [CrossRef]
35. Astanina, M.S.; Buonomo, B.; Manca, O.; Sheremet, M.A. Three-dimensional natural convection of fluid with temperature-dependent viscosity within a porous cube having local heater. *Int. Commun. Heat Mass Transf.* **2022**, *139*, 106510.

36. Gibanov, N.S.; Sheremet, M.A. The impact of position of the local volumetric heat generating source of a semi-cylindrical shape on heat exchange inside the cavity. *Vestn. Udmurt. Univ. Mat. Mekhanika Komp'yuternye Nayki* **2018**, *28*, 119–130. [CrossRef]
37. Tang, G.H.; Tao, W.Q.; He, Y.L. Simulation of fluid flow and heat transfer in a plane channel using the lattice Boltzmann method. *Int. J. Mod. Phys. B* **2003**, *17*, 183–187. [CrossRef]